



Three differentiation stages of a single magma at Piton de la Fournaise volcano (Reunion hot spot)

Vincent Famin and Benoît Welsch

*Laboratoire Géosciences Réunion, Institut de Physique du Globe de Paris, Université de la Réunion, UMR 7154, CNRS, 15 avenue René Cassin, BP 7151, F-97715 Saint Denis messag CEDEX 9, La Réunion, France
(v.famin@univ-reunion.fr)*

Satoshi Okumura

Department of Earth and Planetary Materials Science, Graduate School of Science, Tohoku University, Sendai 980-8578, Japan

Patrick Bachèlery

Laboratoire Géosciences Réunion, Institut de Physique du Globe de Paris, Université de la Réunion, UMR 7154, CNRS, 15 avenue René Cassin, BP 7151, F-97715 Saint Denis messag CEDEX 9, La Réunion, France

Satoru Nakashima

Department of Earth and Space Science, Graduate School of Science, Osaka University, 1-1 Machikaneyama-cho, Osaka 560-0043, Japan

[1] We present major element and volatile concentration analyses in melt and gas inclusions from two recent picrite eruptions (February 2005 and December 2005) at Piton de la Fournaise volcano (La Reunion Island, Indian Ocean). Combined with literature data, our new data show that the large variability of major element compositions in Piton de la Fournaise lavas may be explained by three depth-dependent differentiation stages of a single transitional parental magma (9–11 wt% MgO; 0.5–0.8 wt% K₂O, and 10–12 wt% CaO). The deepest differentiation (>7.5 km) is controlled by the fractional crystallization of clinopyroxene + plagioclase and yields gabbros and basalts enriched in K and depleted in Ca relative to the parental magma. In a shallower storage zone (<2.5 km), differentiation of the transitional parental magma is dominated by the fractionation/accumulation of Fo_{83–85} olivine phenocrysts, yielding Mg-poor basalts at the top of the reservoir and picrites at the base. In cooling dykes and subsurface pockets (<0.6 km), Mg-poor basalts may themselves evolve into more differentiated melts by clinopyroxene + plagioclase fractionation. The incorporation of dunitic xenocrysts or other xenoliths is not necessary to explain the major element chemical diversity of the volcano. The same superposition of differentiation mechanisms may occur at similar depths in other shield volcanoes.

Components: 11,313 words, 8 figures, 4 tables.

Keywords: melt inclusion; magmatic differentiation; ocean island basalt; Reunion hot spot; olivine; major element.

Index Terms: 1036 Geochemistry: Magma chamber processes (3618); 1065 Geochemistry: Major and trace element geochemistry; 1043 Geochemistry: Fluid and melt inclusion geochemistry.

Received 3 March 2008; Revised 18 August 2008; Accepted 27 August 2008; Published 29 January 2009.

Famin, V., B. Welsch, S. Okumura, P. Bachèlery, and S. Nakashima (2009), Three differentiation stages of a single magma at Piton de la Fournaise volcano (Reunion hot spot), *Geochem. Geophys. Geosyst.*, 10, Q01007, doi:10.1029/2008GC002015.

1. Introduction

[2] A key to understanding hot spot dynamics and Earth's mantle heterogeneity is to study the chemical evolution of ocean island basaltic magmas on their way up to the surface [e.g., *Hauri*, 1992]. Knowing how, where, and when these magmas are affected by differentiation, contamination, or mixing is important to constrain the number and depth of magmatic reservoirs, the composition of the crust hosting those reservoirs, and the composition of the mantle source. The largest chemical variability of ocean island basalts (OIB) is found in the shield-building stage of the volcanoes [*Macdonald and Katsura*, 1964], during which picrites (basalts containing more than 20 volume % olivine), alkali basalts, and silica-rich lavas can erupt simultaneously or in short time intervals. Whether these compositional variations are entirely due to a shallow magmatic evolution, to a mixing between different components, or to a heterogeneous mantle source remains debated [*Hauri*, 1992; *Ren et al.*, 2005; *Sobolev et al.*, 2005]. The way how OIB magmatic evolution can yield such a large range of compositions deserves further clarification.

[3] In this paper, we investigate the major element geochemical evolution of OIBs from Piton de la Fournaise, the active volcano of Reunion Island, Indian Ocean (Figure 1). After 6 years of repose, this volcano is now yielding more than one eruption every 8 months since 1998, providing an extensive record of present-day magmatic products. We analyzed major and volatile element concentrations in olivine-hosted melt inclusions (i.e., droplets of magma trapped in minerals) from two recent picrite eruptions (17 February to 2 May 2005 and 26 December 2005 to 18 January 2006; Figure 1a). Melt inclusions are useful because they provide “snapshots” on the composition of the melt at different stages of the magmatic evolution [e.g., *Sours-Page et al.*, 2002] and not only on the final state of the magma as does bulk rock chemistry. This study uses three “snapshots”: primary melt inclusions (trapped during the crystallization of the host olivines), secondary melt inclusions (trapped in deformation microstructures of the minerals after crystallization), and residual matrix

glasses (in the groundmass). We also analyzed secondary gas inclusions (i.e., secondary inclusions that trapped volatiles instead of melt) to investigate the composition of the gas phase in the magma. By comparing our analyses with published data on Reunion bulk rock, melt inclusion, and matrix glasses, we show that the large range of erupted lavas may be explained by successive, depth-dependent crystal fractionations from a single homogeneous magma. Because the geochemical and eruptive pattern of Piton de la Fournaise bears many similarities with other ocean shield volcanoes, these results contribute to a better understanding of OIB evolution worldwide.

2. Previous Work on Magma Compositions at Piton de la Fournaise

[4] The overall volcanic evolution of Reunion Island [e.g., *Upton and Wadsworth*, 1965; *Ludden*, 1978; *Albarède et al.*, 1997] is similar to that of Hawaii [e.g., *Macdonald and Katsura*, 1964; *Chen and Frey*, 1983], even though Reunion magmas are transitional between the alkalic and tholeiitic fields whereas those in Hawaii are tholeiitic on an alkaline versus silica diagram. Reunion Island is made of two main volcanoes (Figure 1), the now extinct Piton des Neiges and the Piton de la Fournaise currently in the shield building stage (i.e., rapid growth and emission of basaltic products [*Peterson and Moore*, 1987]). The two volcanoes are rather similar in major, trace element and isotopic compositions [*Oversby*, 1972; *Zielinski*, 1975; *Ludden*, 1978; *Fisk et al.*, 1988], except for some discrete variations in radiogenic isotopes [*Luais*, 2004; *Bosch et al.*, 2008]. Piton de la Fournaise has yielded a large range of magmatic products over the past 0.5 Ma, classified into four groups based on their bulk major element composition [*Upton and Wadsworth*, 1965, 1972a; *Ludden*, 1978; *Albarède and Tamagnan*, 1988; *Albarède et al.*, 1997]:

[5] 1. Steady state basalts (SSB), which are transitional basalts of little compositional variability (5–8 wt% MgO; 0.5–1 wt% K₂O; 10–12 wt% CaO, Figure 1b), constitute the most frequently erupted products of the volcano. These magmas

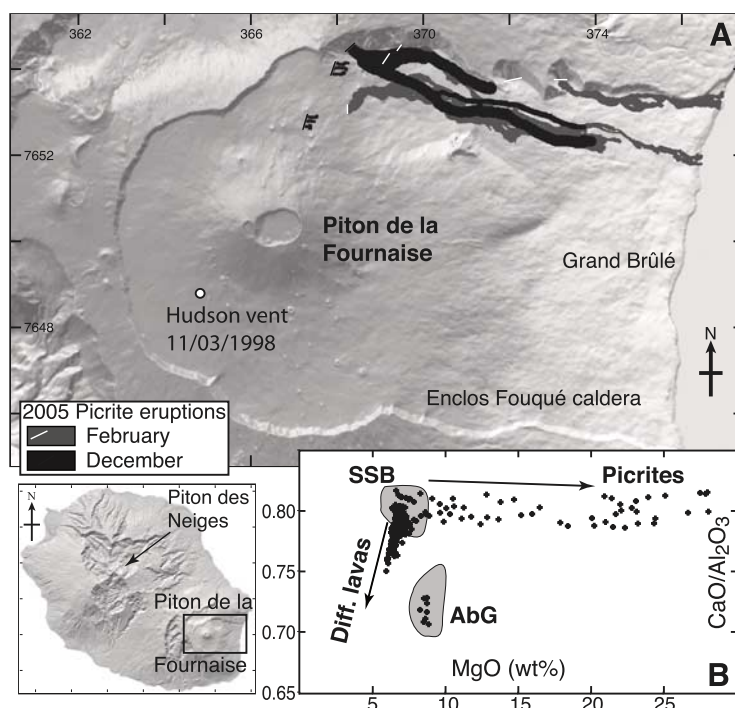


Figure 1. (a) Map of 2005 picrite (basalt containing more than 20 volume % olivine) eruptions on Piton de la Fournaise volcano, Reunion island (Indian Ocean). (b) Bulk-rock major element composition of 1998–2007 eruptive products at Piton de la Fournaise, shown in MgO–CaO/Al₂O₃ space. SSB stands for steady state basalts, AbG for abnormal group basalts, and Diff. Lavas for bennmoreites and mugearites.

mostly erupt near the summit area from dykes rooted at depths of 2 km or shallower [Peltier *et al.*, 2008].

[6] 2. Olivine rich basalts and picrites (5–50 vol% olivine at Fo_{83–85}; 8–28 wt% MgO; 0.4–0.7 wt% K₂O; 5–11 wt% CaO, Figure 1b) are the second most abundant rocks (referred to as “oceanites” in the work of Lacroix [1936]). Picrite eruptions are most often associated with high eruption rates and large volumes of products [Kornprobst *et al.*, 1979]. These lavas are more frequently erupted outside of the summit zone in the lower parts of the volcano. In particular, the two picrite eruptions investigated here (February 2005 and December 2005) occurred more than 4 km away from the summit, on the northeastern side of Piton de la Fournaise (Figure 1a). The elevation of the vents ranged from 1650 to 500 m during the February 2005 eruption and from 2025 to 1600 m during the December 2005 eruption. On the basis of ground deformation modeling and the location of earthquake swarms, dykes were estimated to originate from a depth of 2–2.5 km for these two eruptions [Peltier *et al.*, 2008].

[7] 3. Differentiated, alkaline lavas (1–5 wt% MgO; 1–4 wt% K₂O; 1.8–10 wt% CaO, Figure 1b) are

found mostly in the early stages of Piton de la Fournaise building history and correspond to very rare shallow magmatic activity [Albarède *et al.*, 1997].

[8] 4. In addition, an abnormal group (AbG) of lavas (7.5–10 wt% MgO; 0.9–1.2 wt% K₂O; 8.5–10 wt% CaO), enriched in Mg, Fe, Ti, Na, K, and depleted in Ca, Si relative to SSB (Figure 1b), is represented by a few eruptions on the distal flanks of the edifice and by the recent central eruption of the Hudson vent in 1998 (Figure 1a). Both geochemistry and the location of earthquake swarms indicate that these magmas rise from a depth greater than 7.5 km [Bureau *et al.*, 1998b, 1999; Battaglia *et al.*, 2005b].

[9] Crystalline intrusive products are limited on Piton de la Fournaise and consist of gabbroic or dunitic cumulates. These cumulates are found as xenoliths in lavas [Upton and Wadsworth, 1972b] or in ashes from the 4.7 ka Bellecombe explosive eruption [Mohamed-Abchir *et al.*, 1998; Upton *et al.*, 2000], and as larger bodies sampled by drilling in the Grand Brûlé slope [Rançon *et al.*, 1988]. It is worth noting that on the more eroded Piton des Neiges, a kilometer-scale gabbro crops out in the cirque of Salazie [Upton and Wadsworth, 1972b; Chevallier and Vatin-Perignon, 1982].

[10] Whole rock compositions define two trends in binary diagrams of MgO versus CaO/Al₂O₃ or compatible versus incompatible major elements (Figure 1b), as observed on other ocean shield volcanoes [e.g., Rhodes, 1988]: The low MgO (<7 wt%) trend is controlled by differentiation of the SSB into bennmoreites and mugearites, consisting in the removal of 0–70% in volume of a gabbroic cumulate composed of 20–40% plagioclase, 50–70% clinopyroxene, and ≤10% olivine [Albarède et al., 1997]. The second higher MgO (>7 wt%) trend is due to variable olivine content from SSB (≤5%) to picrites (up to 50%). Using mass balance calculation, early workers have interpreted this trend to be caused by fractionation of 5–10% of olivine (Fo₈₄) from a parental magma at 9–11 wt% MgO; 0.5–0.8 wt% K₂O; 10–12 wt% CaO [Tilley et al., 1971; Ludden, 1978], yielding SSB by depletion on one side and picrites by accumulation on the other side [Clocchiatti et al., 1979]. This parental magma would itself be derived from a primitive magma with 15–17 wt% MgO; 0.4 wt% K₂O; 8–9 wt% CaO issued from partial melting of mantle peridotites [Fisk et al., 1988]. More recently, a xenocryst origin has been proposed for the olivines [Albarède and Tamagnan, 1988; Albarède et al., 1997] because crystals are deformed and their Mg/Fe is in disequilibrium with the groundmass (olivines precipitated from the groundmass melt should have a Fo_{78–81} composition, which is only observed on the rim of crystals). In this interpretation, the olivine trend would be due to the incorporation of genetically unrelated dunites into the SSB during their ascent. The AbG, which lie outside of the two trends, have been interpreted to result from wehrlitic fractionation [Kornprobst et al., 1979].

[11] Recently, some minor variations in trace element concentrations and Pb isotopes have been evidenced in SSB and picrites from the period 1998–2006, indicating some contamination of the magmas by the oceanic crust [Vlastélic et al., 2005; Vlastélic et al., 2007].

3. Sample Description

[12] Samples were taken on 25 February 2005 and 6 January 2006, 9 and 15 days after the beginning of the February and December eruptions, respectively. The samples were collected from the lava flows at ~1100°C (measured with a thermocouple dipped in the flows) and quenched in water.

[13] The samples display the typical petrographic features of picrites erupted on the Piton de la Fournaise, already described in previous studies [Clocchiatti et al., 1979; Albarède and Tamagnan, 1988; Bureau et al., 1998a, 1998b]. They contain 15–40 volume % of polyhedral olivine macrocrystals 0.5–5 mm in diameter, embedded in a groundmass of plagioclase + clinopyroxene ± olivine microlithes and residual matrix glass.

[14] Olivine macrocrystals contain brown, spherical, or ovoid melt inclusions 5–150 μm in diameter (Figure 2a), occurring alone or in random clusters within the crystals. These features indicate that the melt inclusions are primary in origin, i.e., trapped during the crystallization of the host olivine [Roedder, 1979]. Faure and Schiano [2005] have shown that such primary inclusions in polyhedral macrocrystals are trapped in chemical equilibrium with their host olivine. The primary melt inclusions show no evidence for postentrapment modification such as leaking (i.e., loss of matter) or necking down (i.e., change of shape) [Roedder, 1984; Schiano et al., 2006]. These primary melt inclusions contain no visible daughter mineral but occasionally show a shrinkage bubble devoid of any detectable volatiles (see below). In addition, chromium spinels may be observed filling some melt inclusions in variable proportion with the melt or as solid inclusions within the olivines (Figure 2a). These features confirm that spinels were trapped as solid minerals and were not precipitated from the melt inclusions after entrapment as true daughter minerals [Roedder, 1984].

[15] Olivine macrocrystals occasionally display healed cracks and undulose extinction in cross-polarized light, indicating intracrystalline deformation. Healed cracks are microfractures filled with fluids (melt and/or volatiles) and sealed by recrystallization on the walls of the crack, leaving a plane of fluid inclusions. These inclusions are therefore secondary in origin, i.e., trapped after the crystallization of the host olivine. The secondary inclusions are <5–100 μm in diameter and have an oblong or irregular shape (Figure 2b). These secondary inclusions contain pure CO₂ (i.e., gas inclusions) or a mixture of brown glass + CO₂ gas ± spinel (i.e., melt inclusions) in variable gas/melt volume proportions. This indicates that the magma was multiphase and supersaturated in CO₂ at the time of olivine deformation and entrapment.

[16] Embayments filled with brown glass are occasionally observed at the edges of olivine macrocrystals (Figure 2a). The matrix glass between

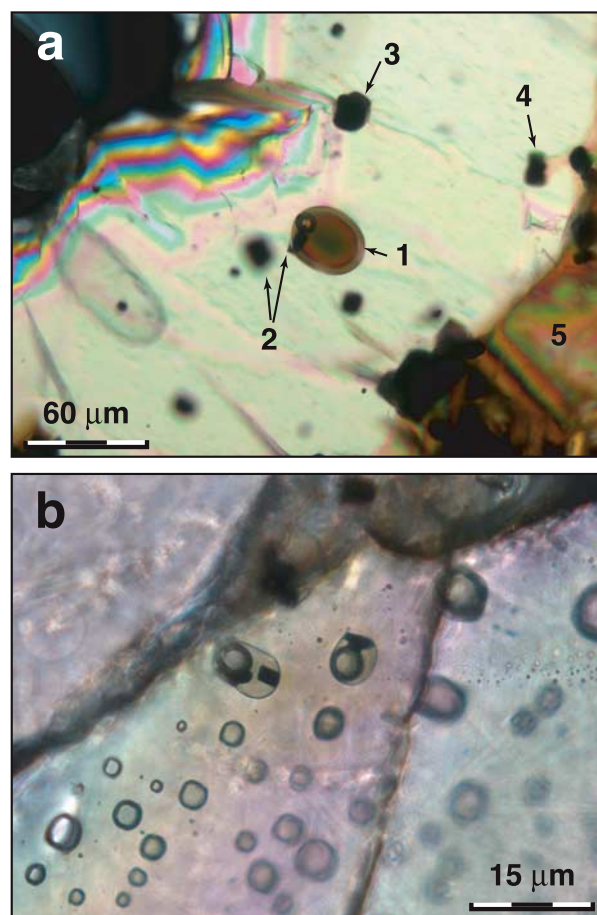


Figure 2. Optical microphotographs (plain light) of olivine-hosted inclusions and matrix glasses in picrites from the 2005 eruptions at Piton de la Fournaise. (a) Several objects are shown on this picture: 1. spherical primary inclusion containing brown melt and a shrinkage bubble; 2. euhedral spinels trapped as solid inclusions (slightly out of focus); 3. spinel inclusion with a rim of brown melt; 4. embayment containing spinels and brown melt; 5. brown matrix glass. (b) Plane of secondary inclusions containing $\text{CO}_2 \pm \text{melt} \pm \text{spinel}$ in variable gas/melt proportions.

microlithes is also brown and contains no visible microcrystals under the microscope.

4. Analytical Methods

[17] Major element analyses of minerals and melt inclusions were carried out on polished thin sections using an electron probe microanalyzer (EPMA) during two analytical sessions. The same operating conditions were used for olivine, spinel, and glass analyses. In the first session, 11 elements analyses were performed on a JEOL JXA-733 (University of Osaka), tuned at 15 kV, 12 nA,

focused beam, 10 s counting times. The following minerals and oxides were used as standards for the elements cited in brackets: albite (Na), orthoclase (K), Fe_2O_3 (Fe), MnO (Mn), quartz (Si), Al_2O_3 (Al), wollastonite (Ca), MgO (Mg), Cr_2O_3 (Cr), NiO (Ni), TiO_2 (Ti). The focused beam allowed the analysis of small ($\sim 15 \mu\text{m}$) melt inclusions, with the drawback of alkali loss [e.g., Morgan and London, 1996]. In the second session, 12 elements analyses were performed on a CAMECA SX100 (Service Camparis, Paris VI University) tuned at 15 kV, 10 nA, beam defocused at $10 \mu\text{m}$, with a 5 s counting time for Na (measured first) and 10–20 s counting times for other elements. The CAMECA set of standards (synthetic and natural minerals or oxides) was used for calibration. In both sessions, the correction methods of Bence and Albee [1968] were used to convert the raw intensity data to weight percent oxides. Analytical uncertainty is 1–2% for major elements, 5–15% for minor elements, and 50–100% for trace elements (average 1σ analytical uncertainty over the two sessions in wt%: 0.58 on SiO_2 , 0.25 on Al_2O_3 , 0.77 on FeO_{tot} , 0.32 on MgO, 0.24 on CaO; 0.29 on TiO_2 , 0.16 Na_2O , 0.11 on K_2O , 0.05 on P_2O_5 ; 0.16 on MnO, 0.09 on NiO, 0.08 on Cr_2O_3). Each composition of minerals and melt inclusions was averaged from five measurements on nonoverlapping spots after check of the homogeneity of the analyses. For major and minor elements, the 1σ error on the five measurements was within the analytical uncertainty, except for three melt inclusions that were in this case discarded. Replicate measurements on the same repolished melt inclusions and host olivines (analyses OIE1bIF1 and OIE8IF1 in Table 1) during the two sessions also fell within analytical uncertainty, except for P that was not measured and Na that was probably underestimated by $\sim 1 \text{ wt}\%$ in glasses with the JEOL JXA-733.

[18] After major element analysis, the samples were doubly polished to a final thickness of 30–100 μm in order to make the melt inclusions stand out from their host olivine on both sides of the thin section. Water and carbon concentration measurements were performed on a FTIR microspectrometer (JASCO MFT-2000, University of Osaka), equipped with a MCT detector and a Ge-coated KBr beam splitter. Spectra were measured by collecting 100 scans in the range 6000–700 cm^{-1} with a 4 cm^{-1} resolution, a 10×10 to $20 \times 20 \mu\text{m}$ window aperture and a background air correction. Water and carbon concentrations were determined from the absorbances (i.e., intensities) of the O–H band at 3450 cm^{-1} and the CO_3^{2-} bands at 1530

Table 1 (Sample). Major Element and Volatile Composition of Primary Melt Inclusions in Olivines From Picrite Eruptions in 2005 [The full Table 1 is available in the HTML version of this article]

REU050225 JEOL JXA-733														CAMECA SX100				
Inclusion	OIA2IF1	OIB1IF1	OIA3IF1	OID1IF1	OIE5IF1	OIE1IF1	OIE4IF1	OIE4IF1	OIE4IF1	OIE4IF1	OIC1IF1	OIC4IF1	OIE1bIF1	OIE1bIF2	OIE6IF1	OIE6IF2	OIE8IF1	OIE8IF2
Diameter (μm)	25	55	15	90	120	130	130	130	115	20	145	55	45	35	60	40	55	85
SiO ₂	50.14	51.38	49.15	51.27	50.39	51.24	51.44	51.99	50.99	50.75	50.47	49.94	49.88	49.88	50.53	50.94	49.70	49.27
TiO ₂	3.01	2.83	3.11	2.87	3.09	2.58	2.70	2.66	2.29	2.89	2.75	2.84	3.18	3.18	2.76	3.12	2.79	2.72
Al ₂ O ₃	15.40	15.47	15.31	15.34	15.47	15.57	15.64	14.94	15.12	15.49	15.48	15.15	15.32	15.32	14.97	15.38	15.17	14.37
Cr ₂ O ₃ ^a	0.04	0.05	0.05	0.05	0.04	0.03	0.03	0.07	0.06	0.06	0.09	0.02	0.62	0.62	0.05	0.00	0.04	0.03
FeO _{tot}	9.83	9.23	9.16	11.53	9.64	10.14	9.54	10.04	8.75	10.35	8.79	10.66	11.50	11.11	9.63	10.94	12.15	12.15
MnO ^a	0.20	0.19	0.13	0.17	0.20	0.21	0.15	0.20	0.19	0.15	0.17	0.18	0.18	0.18	0.22	0.05	0.19	0.11
MgO	4.91	5.25	5.08	5.13	5.27	4.28	5.62	5.40	4.82	5.46	4.80	5.64	5.48	5.48	5.61	4.72	5.81	6.22
NiO ^a	0.01	0.03	0.03	0.01	0.00	0.01	0.03	0.04	0.01	0.06	0.03	0.04	0.07	0.07	0.00	0.04	0.02	0.00
CaO	12.07	12.43	12.05	11.54	11.60	12.38	11.79	11.20	12.16	11.92	12.23	13.94	11.61	11.61	12.66	14.39	13.50	13.08
Na ₂ O	0.99	1.15	0.96	1.55	1.03	1.11	1.37	1.28	1.67	1.32	1.35	2.56	2.68	2.68	2.82	2.68	2.80	2.54
K ₂ O	0.76	0.66	0.83	0.78	0.93	0.73	0.74	0.70	0.73	0.75	0.78	0.84	0.75	0.75	0.74	0.75	1.02	0.80
P ₂ O ₅ ^a	n.a.	n.a.	n.a.	n.a.	n.a.	n.a.	n.a.	n.a.	n.a.	n.a.	n.a.	n.a.	0.42	0.32	0.32	0.77	0.27	0.32
H ₂ O ^a	0.51	0.26	n.a.	0.09	0.34	0.44	0.74	0.62	n.a.	0.77	0.51	0.36	n.a.	n.a.	n.a.	n.a.	0.80	n.a.
CO ₂ (ppm) ^a	66	39	n.a.	b.d.l.	41	b.d.l.	73	64	n.a.	88	40	27	n.a.	n.a.	n.a.	n.a.	77	n.a.
Total (wt%)	97.88	98.94	95.87	100.33	97.99	98.70	99.80	99.14	96.77	99.99	97.46	102.60	101.58	101.80	102.47	103.06	101.61	101.61
<i>Composition of the Host Olivine</i>																		
Cr ₂ O ₃ ^a	0.07	0.04	0.08	0.06	0.06	0.05	0.12	0.00	0.03	0.01	0.05	0.00	0.00	0.00	0.00	0.01	0.01	0.01
NiO ^a	0.20	0.25	0.29	0.33	0.25	0.29	0.29	0.31	0.30	0.23	0.33	0.16	0.16	0.16	0.23	0.23	0.23	0.23
Fo (mol%) ^b	85.3	85.0	85.0	85.1	84.8	84.1	84.4	84.4	84.6	84.3	84.8	84.0	84.0	84.0	84.7	84.7	84.4	84.4
<i>Ol/Sp/liq Equilibrium</i>																		
Mg# sp ^c	0.55	0.55	0.55	0.55	0.54	0.533	0.51	0.539	0.544	0.53	0.535	0.514	0.514	0.514	0.547	0.547	0.529	0.529
Fe ²⁺ /Fe ³⁺ sp ^d	1.96	1.94	1.94	1.95	1.92	1.86	1.81	1.89	1.91	1.88	1.92	1.85	1.85	1.85	1.92	1.92	1.89	1.89

^a Values in bold are below the detection limit of EPMA measurements on trace elements, which is 0.14 wt% on MnO, 0.22 wt% on NiO and 0.15 wt% on Cr₂O₃ in average over the two analytical sessions. Here b.d.l. is concentrations below the detection limit of the FTIR technique (20 ppm for CO₂ and 100 ppm for H₂O) that are treated as zero values in computations, and n.a. is not analyzed.

^b Forsterite content of the host olivine = $100 \times [\text{Mg}]/[\text{Mg} + \text{Fe}^{2+}]$.

^c Mg number of spinel inclusions = $100 \times [\text{Mg}]/[\text{Mg} + \text{Fe}^{2+}]$.

^d Molar ratio of divalent over trivalent iron in the spinel, calculated using the Spincalc Excel sheet [Barnes and Roeder, 2001].

^e Molar ratio of divalent over trivalent iron in the melt, computed using the method of Maurel and Maurel [1982].

^f Uncorrected Mg number of melt inclusions = $100 \times [\text{Mg}]/[\text{Mg} + \text{Fe}^{2+}]$.

^g Fraction of olivine crystallized on the inclusion walls after entrapment, computed as the quantity of host olivine (at a given Fo) that must be added to the melt inclusion to satisfy the condition $K_D = (\text{MgO}/\text{FeO})_{\text{olivine}} = 0.306$ [Fisk et al., 1988]. See Bureau et al. [1998b] for a complete description of the method.

^h Recalculated Mg number of melt inclusions after correction for epitaxial crystallization of olivine = $100 \times [\text{Mg}]/[\text{Mg} + \text{Fe}^{2+}]$.

ⁱ Crystallization temperature of the host olivine using the Helz and Thornber [1987] geothermometer, based on the MgO content of the liquid. The thermometer is calibrated on Kilauea lavas that are similar in major and volatile element compositions to the picrites of Piton de la Fournaise.

^j Pressure of melt inclusion entrapment based on the pressure and temperature dependence of H₂O-CO₂ solubility and estimated using the VolatileCalc software [Newman and Lowenstein, 2002].

and 1430 cm^{-1} , after linear baseline correction. The Beer-Lambert law was used to calculate the concentrations from the absorbances:

$$C = 100.A.M/(\varepsilon.\rho.d),$$

where C is the concentration (wt%), A is the absorbance (dimensionless), M is the molar mass (g mol^{-1}), ε is the molar absorptivity ($\text{L mol}^{-1}\text{ cm}^{-1}$), ρ is the density of the glass (g cm^{-3}), and d is the thickness of the melt inclusion (cm). The value of ε was taken equal to $64\text{ L mol}^{-1}\text{ cm}^{-1}$ for H_2O and $398\text{ L mol}^{-1}\text{ cm}^{-1}$ for CO_3^{2-} [Ihinger *et al.*, 1994]. The value of d was taken equal to 2.8 g cm^{-3} in order to be consistent with previous melt inclusion studies on Piton de la Fournaise [Bureau *et al.*, 1998a; Bureau *et al.*, 1998b; Bureau *et al.*, 1999]. The value of d was measured by Laser scanning confocal microscope (KEY-ENCE, Color Laser 3D Profile Microscope VK-8500 and VK 8510, University of Osaka) with a precision of $\pm 1\text{ }\mu\text{m}$. The uncertainty on concentration estimates is of about 10%. The detection limit for H_2O and CO_2 is of 100 ppm and 20 ppm, respectively.

[19] Because an olivine rim may have crystallized on the walls of melt inclusions after entrapment, the composition of primary melt inclusions was corrected for possible epitaxial olivine crystallization using the olivine-spinel-melt chemical equilibrium, a procedure outlined by Bureau *et al.* [1998b]. Results are therefore presented both before and after correction. This procedure was not applied to secondary melt inclusions because the assumption of melt-olivine chemical equilibrium is not valid in their case.

[20] The composition and density of volatiles in secondary gas inclusions and in the bubble of primary and secondary melt inclusions were determined using a Raman spectrometer (University of Osaka), equipped with an optical microscope (Olympus BX60) and an Ar⁺ ion laser (514.5 nm, 40 mW). A 1200 lines/mm was used. The Raman shift was calibrated using a standard sample of naphthalene. The spectral resolution was 1.5 cm^{-1} . The density of secondary gas inclusions was determined using the technique of Kawakami *et al.* [2003] based on the dependence of the CO_2 Raman spectrum on its density. The two Fermi diad bands of CO_2 (ν^+ at about 1388 and ν^- at 1285 cm^{-1}) were fitted to a Lorentzian curve to determine their peak position (no smoothing was applied to the spectra prior to peak fitting). The density of the

CO_2 in gas inclusions (g cm^{-3}) was then computed using the empirical relationship

$$d = -0.03238697\Delta^3 + 10.08428\Delta^2 - 1046.189\Delta + 36163.67$$

where Δ designates the Fermi resonance splitting between the upper and lower bands of CO_2 ($\Delta = \nu^+ - \nu^-$). The uncertainty on Δ and on the coefficients of the empirical relationship propagates a 1σ error on density estimates of about 0.03 g cm^{-3} [Kawakami *et al.*, 2003].

5. Results

[21] The composition of olivines, spinel inclusions, melt inclusions, and interstitial glasses is reported in Tables 1, 2, and 3. Major element concentrations in glasses are also plotted on Figure 3. Olivines from the February 2005 eruption ($\text{Fo}_{84-85.5}$, peak at $\text{Fo}_{84.5}$) and from the December 2005 eruption ($\text{Fo}_{82-84.5}$, peak at Fo_{84}) are similar in composition to those in previously erupted picrites from Piton de la Fournaise [Clocchiatti *et al.*, 1979; Albarède and Tamagnan, 1988; Bureau *et al.*, 1998a; Bureau *et al.*, 1998b]. Chromium spinel inclusions from the February 2005 eruption ($\text{Mg} \# = 0.51$ to 0.56) are enriched in Mg relative to those from the December 2005 eruption ($\text{Mg} \# = 0.48$ to 0.54). The positive correlation between the Mg content of spinel inclusions and the forsterite content of their host olivines indicate that they are in chemical equilibrium (Table 1). Since primary melt inclusions are trapped together with spinels during olivine crystallization, it is likely that primary melt inclusions are also in equilibrium with the host olivines. This is supported by the polyhedral texture of olivines that have been shown to trap equilibrium melt compositions [Faure and Schiano, 2005]. Primary melt inclusions of both eruptions show a transitional basaltic composition at 8.4–11.1 wt% MgO, 0.40–1.08 wt% K_2O , and 9.8–13.6 wt% CaO, after correction of epitaxial olivine crystallization (8 to 14 mol%) on the inclusion walls (Table 1 and Figure 3). Secondary melt inclusions display a more evolved and scattered composition at 3.3–6.9 wt% MgO, 0.15–1.42 wt% K_2O , and 10.5–14.1 wt% CaO (Table 2 and Figure 3). Note, however, that secondary melt inclusions might appear more evolved than they truly are because epitaxial olivine crystallization might have occurred on their walls but cannot be corrected. No relationship between the size and the composition of melt inclusions is observed (Table 1). Interestingly, the composition of second-

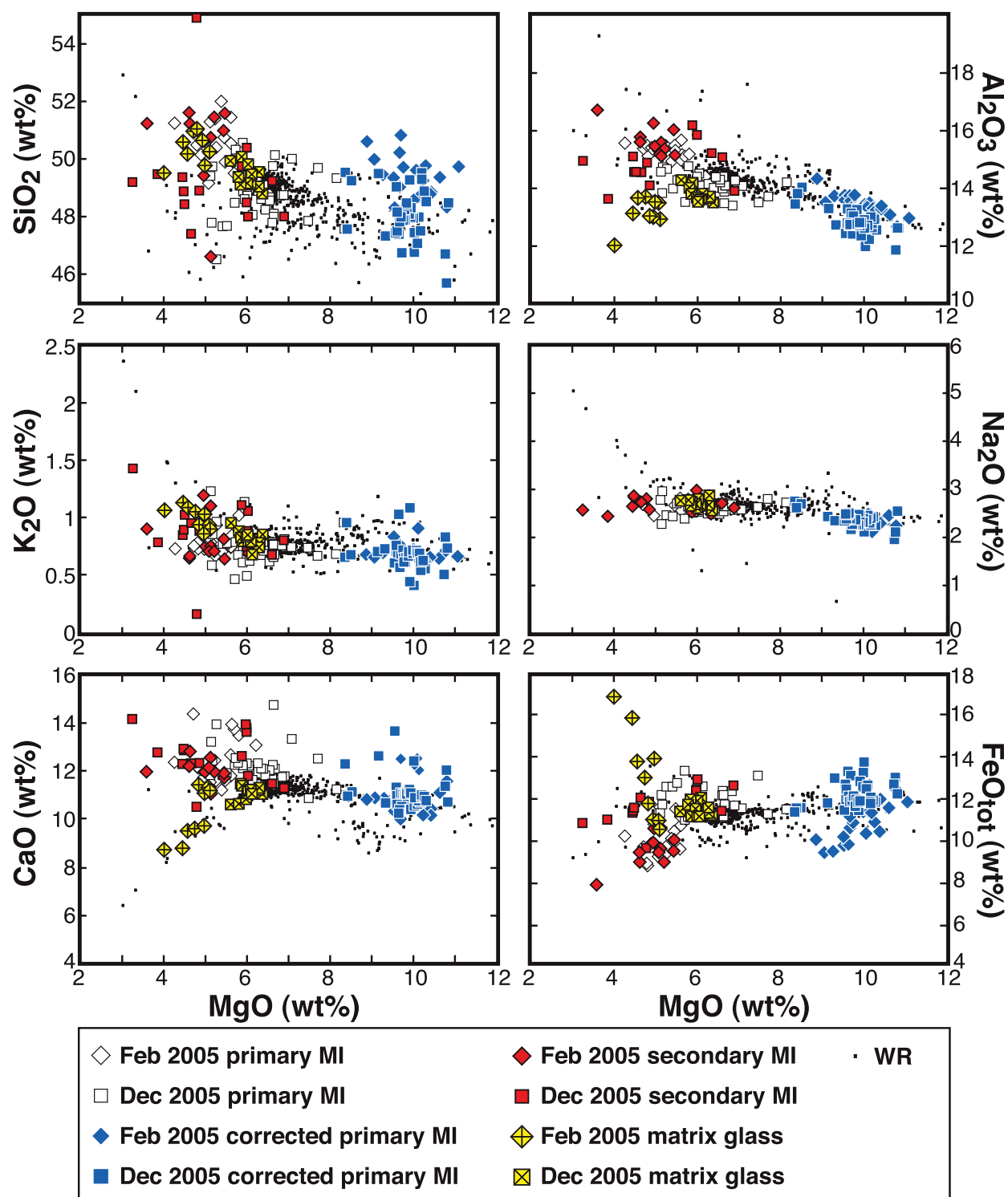


Figure 3. Major element composition of olivine-hosted melt inclusions from the February and December 2005 eruptions. Diamond and squares are for the February 2005 and December 2005 eruptions, respectively. Empty symbols represent primary melt inclusions prior to correction for epitaxial olivine crystallization. Blue symbols are used for primary melt inclusions after correction. Red symbols are for secondary melt inclusions (without correction), and yellow crossed symbols for matrix glasses. Pin points represent the bulk rock composition of Piton de la Fournaise magmatic products [Upton and Wadsworth, 1965; Tilley *et al.*, 1971; Upton and Wadsworth, 1972a; Ludden, 1978; Albarède and Tamagnan, 1988; Fisk *et al.*, 1988; Rançon *et al.*, 1988; Albarède *et al.*, 1997; Mohamed-Abchir *et al.*, 1998; Peltier *et al.*, 2008].

Table 2. Major Element and Volatile Concentrations in Secondary Melt Inclusions Trapped in Olivines From the 2005 Piorite Eruptions

Inclusion Diameter (μm)	OIA3IF5	OIA3bisIF3	OIE3IF1	OIE4IF2	OIE4IF3	OIE4IF6	OIE4IF4	OIE4IF5	OIE4IF2	OIE4IF5	OIE4IF3	OIE4IF4	OIE4IF5	OIE4IF2	OIE4IF4	OIE4IF5	OIE4IF3	OIE4IF4	OIE4IF5	OIE4IF2	OIE4IF4	OIE4IF5	OIE4IF2	OIE4IF4	OIE4IF5	OIE4IF2	OIE4IF4	OIE4IF5
SiO ₂	50.99	51.23	50.61	46.59	51.22	50.74	51.59	51.46	50.20	51.59	49.43																	
TiO ₂	3.13	3.22	2.45	5.82	2.58	3.46	2.57	2.68	2.31	2.71	3.38																	
Al ₂ O ₃	16.03	16.73	15.48	15.12	15.78	15.60	15.61	15.37	15.18	15.16	16.28																	
Cr ₂ O ₃ ^a	0.03	0.05	0.05	0.10	0.07	0.04	0.02	0.03	0.05	0.03	0.06																	
FeO _{tot}	9.44	7.77	10.53	10.61	8.91	9.55	9.37	8.90	9.39	9.97	9.85																	
MnO ^a	0.17	0.14	0.18	0.15	0.20	0.17	0.14	0.14	0.18	0.22	0.09																	
MgO	5.45	3.60	4.98	5.13	4.63	5.13	4.63	5.22	5.09	5.46	4.96																	
NiO ^a	0.01	0.03	0.04	0.06	0.03	0.03	0.05	0.03	0.03	0.03	0.01																	
CaO	11.92	11.98	11.98	12.57	12.83	11.06	12.21	12.00	12.16	11.73	11.25																	
Na ₂ O	0.92	1.11	1.79	1.58	1.47	1.43	1.33	1.70	1.62	1.33	1.52																	
K ₂ O	0.81	0.90	0.75	0.75	0.66	1.10	0.64	0.70	0.70	0.64	1.19																	
P ₂ O ₅ ^a	n.a.	n.a.	n.a.	n.a.	n.a.	n.a.	n.a.	n.a.	n.a.	n.a.	n.a.																	
H ₂ O ^a	n.a.	n.a.	0.05	0.12	0.23	0.07	0.21	n.a.	0.37	n.a.	0.03																	
CO ₂ ^a (ppm)	n.a.	n.a.	b.d.l.	b.d.l.	45	b.d.l.	71	n.a.	b.d.l.	n.a.	b.d.l.																	
Total (wt%)	98.89	96.74	98.89	98.61	98.61	98.39	98.38	98.23	97.29	98.87	98.07																	
Cr ₂ O ₃ ^a	0.08	0.08	0.01	0.12	0.12	0.00	0.00	0.06	0.01	0.05	0.05																	
NiO ^a	0.29	0.29	0.20	0.29	0.29	0.31	0.31	0.33	0.23	0.33	0.33																	
Fe ^b (mol%)	85.0	84.9	85.4	84.4	84.4	84.4	84.4	84.6	84.3	84.8	84.8																	

Inclusion Diameter (μm)	OIB3IF2	OIB4IF1	OIB5IF3	OIB5IF2	OIB5IF1	OIB12IF2	OIB12IF3	OIB3IF3	OIB4IF2	OIB6IF1	OIB7IF1	OIB2IF1	OIB2IF2	OIB4IF1	OIB4IF2	OIB8IF3
SiO ₂	47.39	49.74	49.19	48.42	50.38	48.48	48.80	54.89	48.89	49.16	49.22	49.36	49.46	47.99	47.98	
TiO ₂	4.39	2.73	3.99	3.69	2.96	3.04	3.45	2.40	2.68	3.05	2.80	3.02	3.28	2.82	2.59	
Al ₂ O ₃	15.21	14.55	16.18	14.94	14.57	14.36	15.84	14.56	14.88	14.09	13.93	15.04	15.09	13.62	13.90	
Cr ₂ O ₃ ^a	0.03	0.03	0.06	0.04	0.03	0.05	0.01	0.02	0.08	0.07	0.12	0.09	0.07	0.11	0.12	
FeO _{tot}	12.03	11.72	10.77	11.57	11.20	12.38	11.40	9.58	11.83	11.49	11.39	11.30	10.96	12.64	12.92	
MnO ^a	0.15	0.25	0.18	0.17	0.14	0.19	0.26	0.13	0.22	0.09	0.14	0.22	0.20	0.23	0.22	
MgO	4.67	5.88	3.27	4.51	6.00	6.00	4.49	4.80	4.86	6.03	6.61	4.46	3.87	6.89	6.03	
NiO ^a	0.04	0.08	0.02	0.01	0.08	0.05	0.05	0.02	0.01	0.00	0.00	0.04	0.06	0.00	0.05	
CaO	12.32	12.62	14.17	12.88	13.92	13.64	12.92	10.52	12.33	10.99	11.48	12.30	12.78	11.29	11.80	
Na ₂ O	2.48	2.72	2.52	2.56	2.82	2.63	2.97	2.85	2.79	2.58	2.58	2.70	2.64	2.43	2.61	
K ₂ O	0.95	1.11	1.42	1.02	0.74	0.88	0.89	0.15	0.88	1.05	0.67	0.84	0.78	0.80	0.70	
P ₂ O ₅ ^a	0.44	0.31	0.24	0.37	0.33	0.42	0.41	0.17	0.35	0.45	0.31	0.36	0.52	0.36	0.33	
H ₂ O ^a	n.a.	n.a.	n.a.	n.a.	0.08	0.10	n.a.	n.a.	n.a.	0.41	0.30	n.a.	0.16	0.26	n.a.	
CO ₂ ^a (ppm)	n.a.	n.a.	n.a.	n.a.	b.d.l.	b.d.l.	n.a.	n.a.	n.a.	b.d.l.	b.d.l.	n.a.	b.d.l.	b.d.l.	n.a.	
Total (wt%)	100.10	101.75	101.99	100.18	103.25	102.21	101.48	100.09	99.81	99.46	99.55	99.73	99.86	99.44	99.25	
Cr ₂ O ₃ ^a	0.00	0.00	0.00	0.00	0.00	0.01	0.01	0.04	0.07	0.05	0.00	0.00	0.00	0.05	0.00	
NiO ^a	0.29	0.21	0.26	0.26	0.26	0.24	0.24	0.30	0.23	0.26	0.21	0.27	0.27	0.27	0.27	
Fe ^b (mol%)	84.1	83.8	84.0	84.0	84.0	83.1	83.1	83.5	83.1	84.1	84.0	84.4	84.4	83.0	83.0	

^a Values in bold are below the detection limit of EPMA measurements (see Table 1). Here b.d.l. is concentrations below the detection limit of the FTIR technique and n.a. is not analyzed.
^b Forsterite content of the host olivine = $100 \times [\text{Mg}]/[\text{Mg} + \text{Fe}^{2+}]$.

Table 3. Major Element Composition of Embayments and Interstitial Glass in the Picrites From the February and December 2005 Eruptions

Inclusion	Matrix62	Matrix63	Matrix64	Matrix65	Matrix66	Fracture67	Matrix83	Matrix84	Matrix85	GL 106	GL 109	GL 64/3	GL 64/4	GL 64/5	GL 64/6	GL 64/7	GL 64/2	GL 37/1	GL 33/1	GL 104	GL 105
SiO ₂	50.18	51.02	50.71	50.58	49.59	51.11	50.26	49.83	50.23	49.54	49.81	49.37	49.15	49.46	49.10	49.10	49.92	49.03	48.79	50.07	49.30
TiO ₂	3.99	4.18	3.88	3.50	3.56	2.95	2.23	2.23	2.08	2.95	3.06	3.06	3.07	3.02	3.02	3.02	2.94	3.00	3.01	2.91	2.98
Al ₂ O ₃	13.68	13.74	13.56	13.15	12.05	13.07	13.50	13.01	12.95	13.71	13.59	14.02	13.53	13.81	13.62	13.80	14.29	13.67	13.51	14.19	13.68
Cr ₂ O ₃ ^a	0.00	0.00	0.04	0.01	0.00	0.06	0.08	0.00	0.07	0.06	0.02	0.00	0.00	0.03	0.03	0.01	0.00	0.00	0.01	0.03	0.05
FeO _{tot}	13.82	13.05	13.97	15.96	17.01	11.78	10.95	11.00	10.52	11.27	11.12	11.68	11.86	12.01	11.12	11.93	11.34	11.54	11.17	11.10	11.46
MnO ^a	0.19	0.16	0.23	0.25	0.24	0.23	0.21	0.25	0.17	0.15	0.18	0.00	0.00	0.11	0.08	0.13	0.13	0.21	0.20	0.20	0.12
MgO	4.58	4.76	4.98	4.46	4.02	4.85	5.09	4.96	5.11	6.30	6.03	5.80	6.01	6.12	6.09	5.85	5.61	6.29	6.37	5.88	5.98
NiO ^a	0.00	0.03	0.00	0.00	0.00	0.08	0.00	0.00	0.02	0.02	0.00	0.00	0.00	0.09	0.00	0.00	0.00	0.20	0.17	0.00	0.00
CaO	9.56	9.66	9.79	8.84	8.75	11.49	11.26	11.13	11.23	11.37	11.18	10.62	11.06	11.04	11.21	11.45	10.60	11.21	11.03	11.38	10.83
Na ₂ O	1.21	1.26	1.24	1.62	2.43	1.45	1.82	1.89	1.76	2.69	2.79	2.78	2.62	2.66	2.66	2.66	2.76	2.87	2.56	2.74	2.69
K ₂ O	1.10	1.06	1.03	1.13	1.07	0.94	0.94	0.86	0.91	0.78	0.79	0.88	0.85	0.68	0.80	0.83	0.96	0.74	0.86	0.80	0.84
P ₂ O ₅ ^a	0.08	0.08	0.08	0.08	0.08	0.08	0.08	0.08	0.08	0.07	0.07	0.08	0.08	0.07	0.08	0.08	0.07	0.08	0.08	0.08	0.08
H ₂ O ^a	0.08	0.08	0.08	0.08	0.08	0.08	0.08	0.08	0.08	0.07	0.07	0.08	0.08	0.07	0.08	0.08	0.07	0.08	0.08	0.08	0.08
CO ₂ ^a (ppm)	0.08	0.08	0.08	0.08	0.08	0.08	0.08	0.08	0.08	0.07	0.07	0.08	0.08	0.07	0.08	0.08	0.07	0.08	0.08	0.08	0.08
Total (wt%)	98.37	99.00	99.50	99.56	98.80	98.07	96.39	95.24	95.13	99.17	98.92	98.61	98.71	99.36	98.14	99.15	98.93	99.19	98.02	99.69	98.34

^a Values in bold are below the detection limit of EPMA measurements (see Table 1). Here b.d.l. is concentrations below the detection limit of the FTIR technique and n.a. is not analyzed.

ary melt inclusions is similar to the raw composition of primary melt inclusions before epitaxial olivine correction. The most evolved melts are found in matrix glasses and embayments at 4.0–5.1 wt% MgO, 0.86–1.13 wt% K₂O, and 8.7–11.5 wt% CaO (Table 3 and Figure 3).

[22] It has been shown that the major element composition of melt inclusions may be modified after entrapment by Fe-Mg exchange with the host olivine [Danyushevsky *et al.*, 2000; Gaetani and Watson, 2000; Gaetani and Watson, 2002; Danyushevsky *et al.*, 2004]. The result is a significant decrease in FeO and increase in MgO in the trapped melt. However, the total iron content of primary and secondary melt inclusions without correction (8.8–13.4 wt% FeO_{tot}) falls within the scatter of the whole rock FeO_{tot} concentrations, and no evidence for Fe²⁺ loss is observed (Figure 3).

[23] H₂O and CO₂ concentrations in melts are listed in Tables 1, 2, and 3 and reported on Figure 4. The glass phase of primary melt inclusions from the February 2005 eruption contain 0.07–0.67 wt% H₂O and <20–80 ppm CO₂, while that from the December 2005 primary melt inclusions contain 0.06–0.70 wt% H₂O and <20–170 ppm CO₂, after correction for epitaxial olivine crystallization. Neither water nor CO₂ was detected by micro-Raman in the occasional shrinkage bubble of primary melt inclusions. Because the volume of this bubble is less than 5% of the volume of the inclusion, we assume that water and CO₂ concentrations measured in the glass phase are relevant of the melt composition at the time of inclusion entrapment. Secondary melt inclusions from the February 2005 eruption contain 0.03–0.35 wt% H₂O and <20–70 ppm CO₂ while those from the December 2005 eruption contain 0.08–0.67 wt% H₂O and no detectable CO₂. Matrix glasses and embayments contain <0.01–0.08 wt% H₂O and no detectable CO₂. As a general rule, the most water rich melt inclusions are also the most CO₂ rich. Primary melt inclusions contain more H₂O and CO₂ than secondary melt inclusions, which themselves contain more volatiles than matrix and embayment glasses. Note also that primary and secondary melt inclusions become less abundant with increasing H₂O and CO₂ concentration.

[24] Results of micro-Raman spectroscopy are reported on Figure 5. Raman spectra indicate that secondary gas inclusions contain pure CO₂ without any other detectable volatile compound. In the 28 analyzed gas inclusions, the Fermi resonance splitting between the two CO₂ peaks ranges from 102

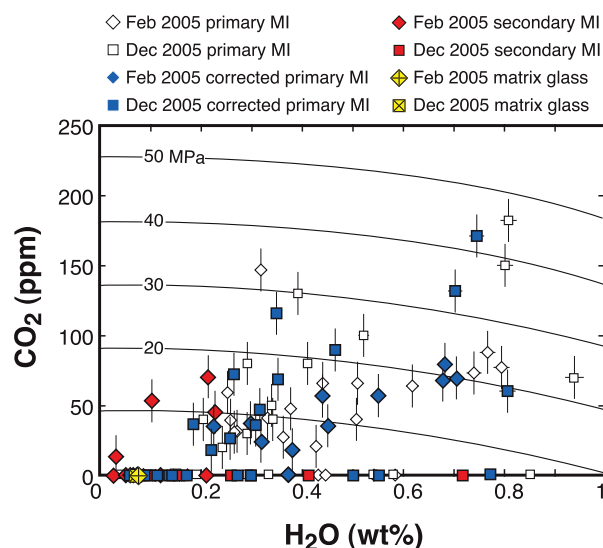


Figure 4. H_2O versus CO_2 concentration in olivine-hosted melt inclusions from the February and December 2005 eruptions. Diamonds represent February 2005 eruption. Squares represent December 2005 eruption. Empty symbols are used for primary melt inclusions without correction, blue symbols for primary melt inclusions after correction for epitaxial olivine crystallization, red symbols for secondary melt inclusions (without correction), and yellow crossed symbols for matrix glasses.

to 103.2 cm^{-1} , or a CO_2 density of 0 to 0.29 g cm^{-3} . Note also that the abundance of gas inclusions decreases with increasing CO_2 density.

6. Discussion

6.1. Depth of Olivine Crystallization in Picrites

[25] Because water and carbon saturation in silicate melts is pressure and temperature dependent, the depth of entrapment of melt inclusions may be estimated from their H_2O and CO_2 concentration. Using the VolatileCalc software [Newman and Lowenstern, 2002] and temperatures given by the Helz and Thornber [1987] thermometer, primary melt inclusions from the two 2005 picrite eruptions are estimated to crystallize in a similar range of depths from ~ 0 to 1600 m (Figures 5 and 6). With the same approach, secondary melt inclusions are estimated to be entrapped at a maximum of 600 m depth (the depth of entrapment of secondary melt inclusions may be overestimated because of uncorrected olivine epitaxial crystallization). Note that for both primary and secondary melt inclusions, the abundance of data decreases with increasing depth.

[26] The depth of entrapment of secondary CO_2 gas inclusions may also be estimated from the density of CO_2 , assuming a 2.8 g cm^{-3} magma density and a 1200°C ambient temperature (the uncertainty on temperature yields only minor error on pressure estimates of CO_2). Consequently, Raman data yield a depth range of 0 to 2200 m for the entrapment of secondary gas inclusions, with one datum at 2600 m depth (Figure 6). Gas inclusions appear to yield slightly greater depths than melt inclusions. Note, however, that the uncertainty of depth estimates from both techniques is about 500 m. In the case of gas inclusions also, the abundance of measurement decreases with increasing depth.

[27] Overall, the two independent data sets both suggest that the growth of olivines in picrites and their transport proceeds at a very shallow depth, limited to a zone shallower than 2600 m below the surface. Our estimate is consistent with the depth of picrite olivine crystallization proposed by Bureau *et al.* [1998b] and also consistent with the depth of picrite dykes modeled from ground deformation [Peltier *et al.*, 2008]. Olivine enrichment in picrites is a shallow process; hence MgO increase in bulk rock should not be taken as an evidence for reservoir recharge by deep magmas such as proposed by Vlastélic *et al.* [2007]. In addition, the decreasing frequency of data with increasing depth indicates that olivines crystallized at shallow level are more abundant in the eruptive products than deeper ones (Figure 6). It is possible that the frequency of data might represent a bias in the incorporation of olivines into the erupted lavas. Another possibility is that the frequency of data represents true abundances in the magma reservoir. In this case, the picrites would collect more olivines crystallized from the (cooler) top of the

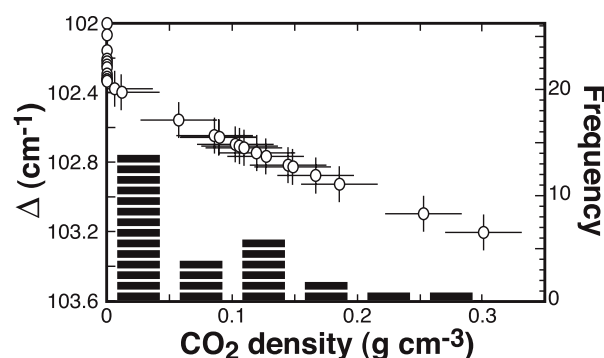


Figure 5. Density of CO_2 -bearing secondary gas inclusions in olivines from the February 2005 eruption. Data are represented as a function of the Fermi resonance splitting (shown by Δ) between the two Raman peaks of CO_2 and also as a frequency histogram.

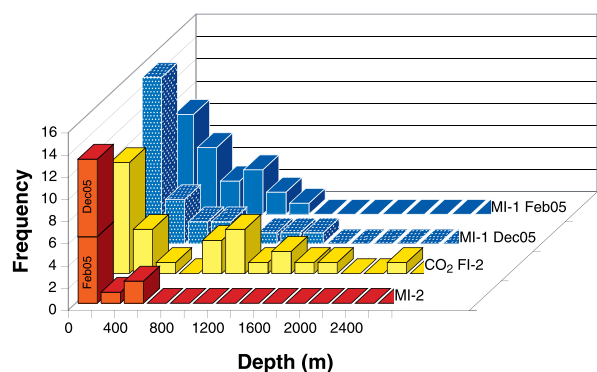


Figure 6. Depth of melt and gas inclusion entrapment in olivines from the February and December 2005 eruptions, estimated using two different types of data: (1) H_2O – CO_2 concentrations in the melt inclusions assuming vapor saturation (blue histogram for February 2005 primary melt inclusions, dotted blue histogram for December 2005 primary melt inclusions, red histogram for secondary melt inclusions); (2) CO_2 density of secondary gas inclusions assuming a 1200°C temperature of entrapment (yellow histogram).

reservoir than from the lower parts. This would be consistent with the interpretation that picrites come from a chemically stratified reservoir [Vlastélic *et al.*, 2005], depleted in Mg at the top by olivine fractionation and proportionally enriched at the base by accumulation.

6.2. Source of Picrites and Steady State Basalts

[28] In Figure 7, the composition of melt inclusions from the two 2005 picrite eruptions is compared with whole rock data on Piton de la Fournaise. Primary melt inclusions from this study show that the most frequently entrapped melts during olivine growth have the composition of the parental magma (9–11 wt% MgO , 0.5–0.8 wt% K_2O , and 10–12 wt% CaO) proposed by Ludden [1978]. Fo_{83-85} olivines from picrite lavas are in equilibrium with primary melt inclusions (Table 1) and therefore with this parental magma. On the other hand, primary melt inclusions after epitaxial olivine crystallization (i.e., without composition correction) and secondary melt inclusions lie in the range of more differentiated SSB (Figures 3 and 7), and would be in equilibrium with Fo_{78-81} olivines such as found on the rims of Fo_{83-85} macrocrystals. Consequently, the composition of SSB and rimmed macrocrystals may be entirely explained by the fractional crystallization of 8–14 mol% of picrite olivines (Fo_{83-85}) from the parental magma. Fo_{83-85} olivines in picrites are

phenocrysts as proposed by Clocchiatti *et al.* [1979] and not xenocrysts derived from the disaggregation of earlier cumulates and incorporated into SSB, as interpreted later [Albarède and Tama-gnan, 1988; Albarède *et al.*, 1997]. We therefore concur with the interpretation that SSB and picrites may evolve from a common magma storage zone (or a complex of connected storage zones) simply by fractional crystallization of Fo_{83-85} olivines [Tilley *et al.*, 1971; Ludden, 1978; Clocchiatti *et al.*, 1979; Kornprobst *et al.*, 1979]. Olivine rims at Fo_{78-81} are in equilibrium with SSB and therefore develop in the differentiated liquid after most of the crystal fractionation. The fact that all the fluid inclusions (primary and secondary, melt or gas) are trapped at a similar shallow depth range (Figure 6), and that secondary melt inclusions have an SSB composition (Figure 7), suggests that picrite olivines grow, travel, and are deformed within a single storage system. This reservoir has the bulk composition of the parental magma [Tilley *et al.*, 1971; Ludden, 1978], but is vertically stratified (between recharge periods) due to fractional crystallization, with a top of SSB composition at a few hundreds meter depth and a bottom of picrite composition at a maximum depth of 2600 m.

6.3. Three Differentiation Histories of a Single Magma

[29] Previously published melt inclusion and matrix glass data have been compiled in Figure 7. Overall, three trends may be observed instead of two:

[30] 1. A first trend (Line 1) is defined by primary melt inclusions (i.e., the parental magma), AbG whole rocks and secondary inclusions trapped in olivines from AbG eruptions (Figures 7a and 7b). In the light of Line 1, AbG may be explained as an evolution of the parental magma by crystal fractionation of a cumulate composed of 20–40 vol% plagioclase, 50–70% clinopyroxene, and $\leq 10\%$ olivine. No gabbroic cumulates of such composition have been found on Piton de la Fournaise. On the more eroded Piton des Neiges (Figure 1), however, the composition of the Salazie gabbro body falls on the trend (Figures 7a and 7b). Since rock chemistry is quite similar at both volcanoes, a gabbro such as found on Piton des Neiges may represent the cumulative counterpart of AbG differentiation (Figures 7c and 8). According to the deep origin of abnormal eruptions [Bureau *et al.*, 1998b; Battaglia *et al.*, 2005a], gabbro accumulation should proceed in a reservoir located at depth

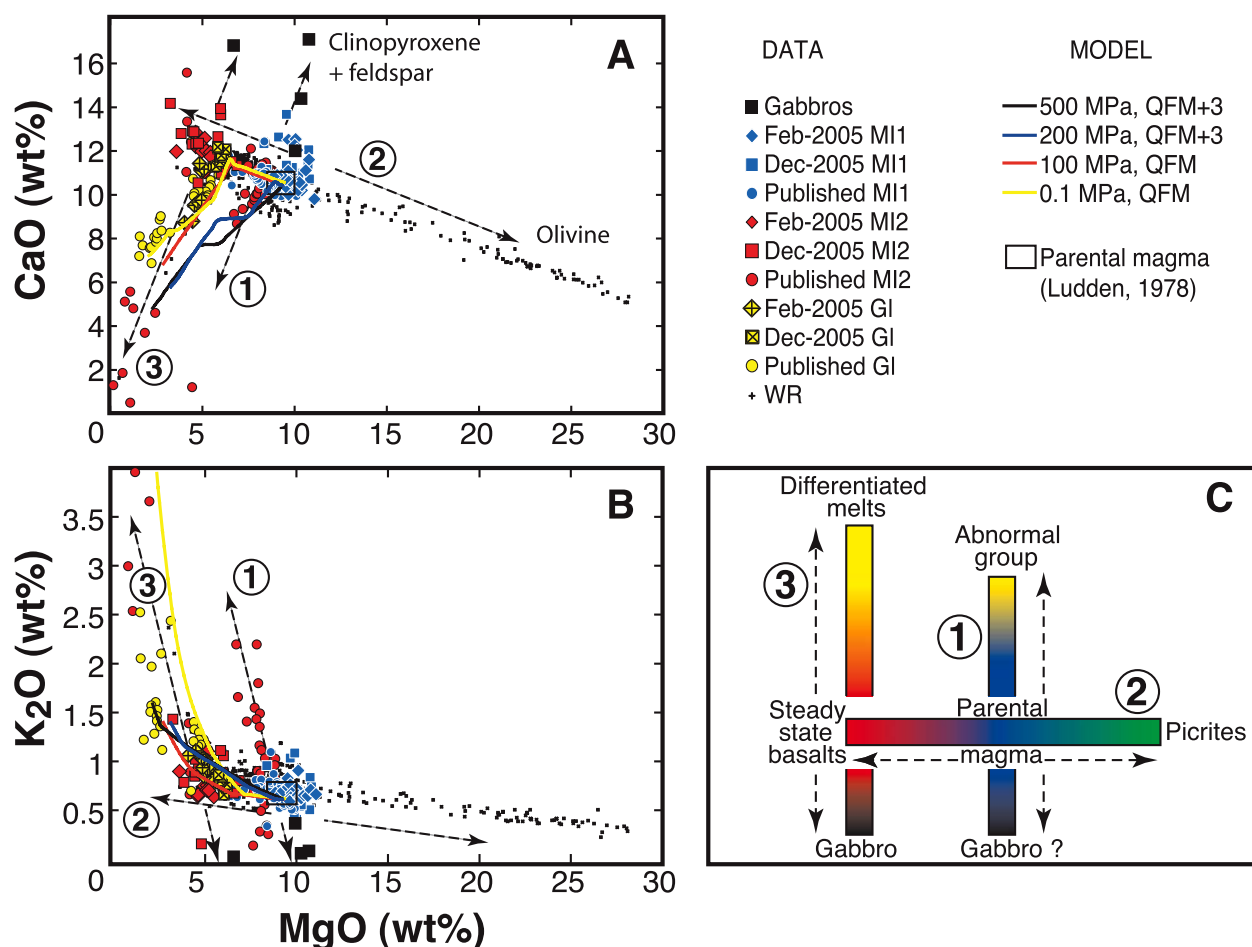


Figure 7. (a–b) Compilation of K₂O and CaO concentrations versus MgO in magmas from Piton de la Fournaise volcano. Pin points represent published whole rock data [Upton and Wadsworth, 1965; Tilley et al., 1971; Upton and Wadsworth, 1972a; Ludden, 1978; Albarède and Tamagnan, 1988; Fisk et al., 1988; Rançon et al., 1988; Albarède et al., 1997; Mohamed-Abchir et al., 1998; Peltier et al., 2008]. Black squares represent the whole rock composition of gabbros from Piton de la Fournaise and Piton des Neiges [Upton and Wadsworth, 1972b; Rançon et al., 1988; Upton et al., 2000]. Blue symbols represent primary melt inclusions, red symbols represent secondary melt inclusions, and yellow symbols represent embayments and matrix glasses. Diamonds and squares represent melt data from the February and December 2005 eruptions, respectively. Circles are used for previously published melt inclusion and interstitial glass data. In this literature data set, primary and secondary melt inclusions were analyzed in picrite and AbG eruptions [Bureau et al., 1998a; Bureau et al., 1998b; Bureau et al., 1999]; interstitial glasses were analyzed in the AbG eruption of Hudson 1998 [Villeneuve, 2000]. The empty box is the parental magma suggested by [Tilley et al., 1971; Ludden, 1978]. Solid lines represent numerical simulations of fractional crystallization from the parental magma based on the MELTS software [Ghiorso and Sack, 1995; Asimow and Ghiorso, 1998]. Input parameters and results are given in Table 4. (c) Interpretative sketch of differentiation sequence at Piton de la Fournaise volcano. Line 1 is explained by plagioclase + clinopyroxene fractionation/accumulation of parental magmas (in blue), yielding “abnormal magmas” (in yellow) and possibly gabbros (in black) of the Piton des Neiges type. Line 2 is explained by olivine fractionation/accumulation of parental magmas, yielding picrites (in green) and steady state basalts (in red). Line 3 is explained by plagioclase + clinopyroxene fractionation/accumulation of steady state basalts, yielding differentiated magmas (in yellow) and gabbroic cumulates (in black) of the Piton de la Fournaise type.

greater than 7.5 km (Figure 8). Differentiated secondary melt inclusions are likely trapped along Line 1 after the fractionation of plagioclase + clinopyroxene ± olivine.

[31] 2. The second trend (Line 2) is defined by primary melt inclusions, by secondary melt inclu-

sions from the two 2005 picrite eruptions and by most of the whole rock data on Piton de la Fournaise (Figures 7a and 7b). As discussed above, Line 2 is the result of both fractionation and accumulation of Fo_{83–85} olivines, yielding SSB on the low MgO side of Ludden’s [1978] parental

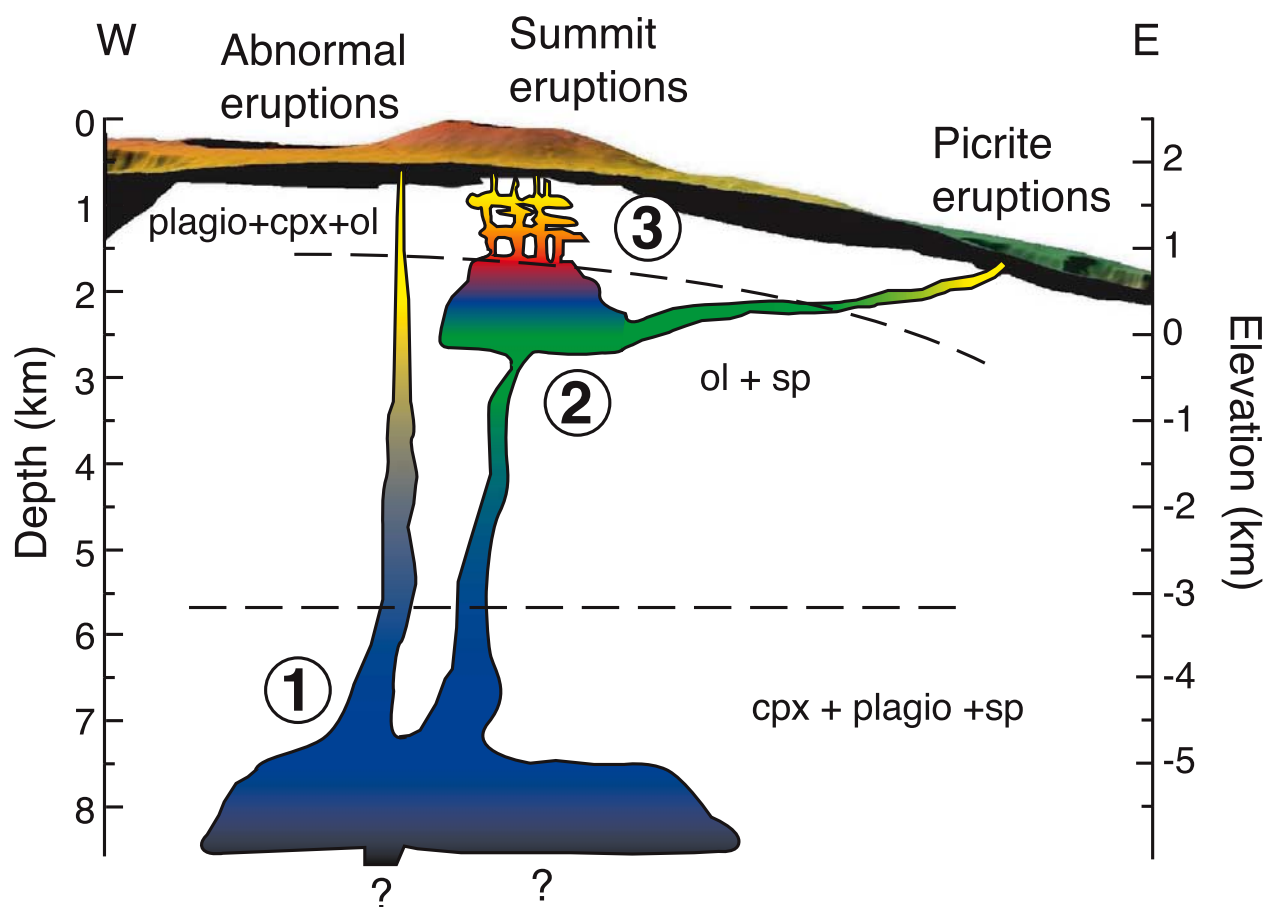


Figure 8. Conceptual geochemical model of magma storage and transport beneath Piton de la Fournaise volcano. (1) Parental magmas (in blue) may occasionally rise directly from a deep reservoir at 7.5 km depth or more. In this case, magmas undergo differentiation by plagioclase + clinopyroxene fractionation (yellow) during their ascent, yielding melts of the “Abnormal Group.” Possibly, gabbros (in black) may accumulate at the base of this reservoir. (2) Most of the parental magma, however, episodically rises through a shallower reservoir at 2–2.5 km depth (or a complex of connected reservoirs) in which it undergoes differentiation by olivine fractionation. Between episodic refills, this reservoir becomes vertically chemically zoned by differentiation, with steady state basalts (in red) at the top and picrites (in green) at the bottom. Dykes originating at the top of this storage complex yield summit eruptions, while dykes originating at the base of the reservoir yield lateral eruptions, as shown by GPS data and earthquake depths [Longpré *et al.*, 2007; Peltier *et al.*, 2008]. (3) Crystallization of plagioclase + clinopyroxene microlithes during magma ascent produces differentiated residual matrix glasses (in yellow) within, steady state basalts, picrites and abnormal basalts at shallow level (<600 m depth). Occasionally, some very shallow pockets of magma may become disconnected from the main storage complex and evolve for longer time by plagioclase + clinopyroxene fractionation, yielding small differentiated eruptions.

magma and picrites on the high MgO side, in a reservoir not deeper than 2.5 km (Figures 7c and 8). This conclusion is in perfect agreement with early studies on Piton de la Fournaise picrites [Tilley *et al.*, 1971; Ludden, 1978; Clocchiatti *et al.*, 1979; Kornprobst *et al.*, 1979].

[32] 3. The third trend (Line 3) is defined by secondary melt inclusions and matrix glasses from shallow rooting eruptions, the most evolved whole rock lavas on Piton de la Fournaise and by xenoliths found in the Bellecombe ashes (Figures 7a

and 7b). Line 3 is subparallel to Line 1 and may therefore also be explained by the differentiation of steady state basalts due to crystallization of plagioclase and clinopyroxene (Figure 7c), as proposed by Albarède *et al.* [1997]. Along this line, the evolved melts in secondary inclusions and matrix glasses may result from microlithe crystallization during the ascent of magmas (at a depth smaller than 600 m as suggested by secondary melt inclusions, Figure 6), without invoking fractional crystallization. Note that all the lavas, including SSB, picrites, and AbG, end up with this step of shallow

Table 4. Numerical Simulations of Fractional Crystallization Using the MELTS Software^a

Pressure ^b (MPa)	log fO ₂ Buffer ^c	Volume % of Solid Crystallized at 1050°C	Mineral Composition of the Solid (vol%) in Order of Crystallization ^d
500	QFM+3	52.1	75 cpx + 13 sp + 12 fs
300	QFM+3	48.47	69 cpx + 16 sp + 15 fs
200	QFM+3	45.99	66 cpx + 18 sp + 16 fs
100	QFM+3	43.16	61 cpx + 20 sp + 17 fs + 2 ol
75	QFM+3	42.61	3 ol + 60 cpx + 20 sp + 17 fs
50	QFM+3	45.94	3 ol + 59 cpx + 21 sp + 17 fs
25	QFM+3	40.99 (+19 % H ₂ O)	3 ol + 49 cpx + 18 sp + 30 fs
0.1	QFM+3	0.44 (+99.4 % H ₂ O)	1 ol + 41 cpx + 48 fs + 10 sp
500	QFM	57.61	92 cpx + 1 sp + 7 fs
300	QFM	54.16	4 ol + 72 cpx + 4 sp + 20 fs
200	QFM	50.79	12 ol + 60 cpx + 6 sp + 22 fs
100	QFM	47.41	18 ol + 50 cpx + 25 fs + 7 sp
75	QFM	46.69	19 ol + 49 cpx + 25 fs + 7 sp
50	QFM	45.94	20 ol + 48 cpx + 25 fs + 7 sp
25	QFM	45.27 (+25 % H ₂ O)	16 ol + 38 cpx + 39 fs + 7 sp
0.1	QFM	0.5 (+99.46 % H ₂ O)	6 ol + 50 fs + 38 cpx + 6 sp

^aFrom Ghiorso and Sack [1995] and Asimow and Ghiorso [1998].

^bAll the runs were performed with a temperature decrease from 1300 to 1050°C. Orthopyroxene was excluded of the possible crystallizing phases because it is not observed in volcanic rocks of Reunion Island. The composition of the initial liquid undergoing fractional crystallization was adapted from Ludden's [1978] parental magma, with a volatile concentration taken equal to the maximum concentration found in Piton de la Fournaise melt inclusions [Bureau et al., 1998b, 1999]: 47.7 wt% SiO₂; 2.7 wt% TiO₂; 13.25 wt% Al₂O₃; 1.6 wt% Fe₂O₃; 10.1 wt% FeO; 0.17 wt% MnO; 9.5 wt% MgO; 0.05 wt% NiO; 10.5 wt% CaO; 2.45 wt% Na₂O; 0.67 wt% K₂O; 0.3 wt% P₂O₅; 1 wt% H₂O; 0.1 wt% CO₂.

^cOxygen fugacity was set at two buffers: Quartz–Fayalite–Magnetite (QFM) and QFM+3 (in log unit).

^dAbbreviations: olivine (ol); clinopyroxene (cpx); spinel (sp); feldspar (fs).

differentiation. Whole rock data suggest, however, that cooling dykes or small subsurface pockets of magma may occasionally become disconnected from the main storage complex and yield fractionation of an assemblage composed of 20–40% plagioclase, 50–70% clinopyroxene, and ≤10% olivine, and small volumes of more differentiated magmas (Figure 8). The cumulative counterpart of this differentiation may correspond to the gabbro xenoliths found in the Bellecombe ashes.

[33] The change from one differentiation line to the next is likely pressure, temperature and compositionally dependent, yet experimental data are too scarce for quantitative phase diagrams to be established. Using published experimental data on SSB [Green and Ringwood, 1967; Fisk et al., 1988], Albarède et al. [1997] have placed the crossover between clinopyroxene-dominant and olivine-dominant crystallization at 0.9 ± 0.2 GPa [Albarède et al., 1997, Figure 21]. However, since the parental magma affected by the first clinopyroxene + plagioclase fractionation (Line 1) is more primitive than the starting magma used in their experimental work, the clinopyroxene-olivine crossover is very likely much shallower than 0.9 ± 0.2 GPa (30 km). Indeed using the MELTS software [Ghiorso and Sack, 1995; Asimow and Ghiorso, 1998], simulations of fractional crystallization from the parental magma above 300 MPa yield an assemblage 69–92 vol%

clinopyroxene + 7–20% feldspar + 1–16% spinel (Table 4). This assemblage is consistent with the average mineral composition of the Salazie gabbro [Upton and Wadsworth, 1972b]. It is only from 280 MPa (10 km) and below that olivine becomes a significant (i.e., >5 vol%) phase in the solid. In MgO–CaO space (Figure 7a), Line 1 is best simulated by liquid lines of descents in the range 200–500 MPa, with the oxygen fugacity set at the quartz-fayalite-magnetite buffer (QFM) + 3 in log unit. These simulations also fit well SiO₂, TiO₂, MnO, Na₂O, and P₂O₅ data but do not fit FeO, Fe₂O₃, Al₂O₃, and K₂O data (Figure 7b). The misfit of FeO and Fe₂O₃ may be caused by a decrease of the redox state at shallow level. Note that for the range of liquid compositions considered here (44–49 wt% SiO₂; 6–10 wt% MgO), the few experimental basaltic liquids available in the calibration database of MELTS at 200–500 MPa are much more aluminous (i.e., 17.29–20.06 wt% Al₂O₃) than our parental magma (at 13.5 wt% Al₂O₃). Therefore, a possible cause of the Al₂O₃ and K₂O misfit is that feldspar crystallizes earlier than predicted by MELTS because the software calibrated on Al₂O₃-rich basaltic liquids underestimates the temperature at which feldspar crystallization begins in Al₂O₃-depleted liquids.

[34] For all the major elements, Line 2 and Line 3 are best fitted by MELTS simulations in the range

0.1–100 MPa with the oxygen fugacity set at the QFM buffer (Figures 7a and 7b). The maximum volume of olivine crystallization (18–19 vol%, Table 4) is obtained at 50–100 MPa (1.8 – 3.5 km), in good consistency with our depth estimate of Line 2 differentiation. Below 25 MPa (0.9 km), the dominant crystallizing phases are feldspar (39–50 vol%) and clinopyroxene (39 vol%), in consistency with Line 3 (Table 4) and with the mineral composition of the gabbroic xenoliths within the Bellecombe ashes [Upton *et al.*, 2000]. The results of MELTS simulations are therefore in general agreement with our interpretation of superimposed differentiation lines. The succession of differentiation mechanisms and liquid major elements composition is mostly controlled by the depth of the magma storage zones.

[35] An essential implication of our findings is that compositional heterogeneities at Piton de la Fournaise may all stem from superimposed differentiation stages of a single homogeneous parental magma. The incorporation of olivine xenocrysts and/or other xenoliths does not likely account for major element variations in lavas. The crustal assimilation evidenced by isotopes and trace elements [Vlastélic *et al.*, 2005; Vlastélic *et al.*, 2007] probably involves small volumes of wall rock that do not affect the chemical diversity of Piton de la Fournaise products and hence cannot be resolved using our major element data.

[36] The recognition of three differentiation zones is in general agreement with geophysical and seismological studies that proposed the existence of three main reservoirs beneath Piton de la Fournaise; a shallow complex of sills and dykes at a few hundreds meter beneath the summit [Lénat and Bachèlery, 1990]; a reservoir at 2–2.5 km depth from which SSB and picrite dykes root [Peltier *et al.*, 2008]; and the starting point of earthquake swarms at 7.5 km depth suggesting deeper magmas transfers [Battaglia *et al.*, 2005a]. Magma ascent being driven by the lower density of the liquid than the wall rock, storage zones probably represent halts of the magma at levels of neutral buoyancy in the crust and upper mantle [Lister and Kerr, 1991]. Beneath Hawaii and Canary islands, Ryan [1988] and Hansteen *et al.* [1998] have proposed that magmas accumulate at two levels of neutral buoyancy, a deep level at 6–10 km depth and a shallower level at 2–4 km. Our study suggests that the two deepest of the three storage zones evidenced at Piton de la Fournaise also lie within the same depth ranges (Figure 8). Because Piton

des Neiges and Mauritius volcanic products are similar in major element composition to those of Piton de la Fournaise [Upton and Wadsworth, 1972a; Debajyoti *et al.*, 2007], it is very likely that a similar superposition of differentiation lines occurred at the same depths (above 7.5 km, below 2.5 km and at the subsurface) during the past activity of these two extinct volcanoes. This reinforces the idea that the depth of storage zones is a constant parameter in OIB dynamics and that two levels of neutral buoyancy are reached beneath shield volcanoes. The deeper level would be controlled by the density of the upper oceanic crust, and the shallower level would be controlled by the density of the volcanic edifice.

7. Conclusion

[37] Our major element and volatile analyses of melt and gas inclusions from recent picrite eruptions, together with data from the literature, provide new constraints on OIB dynamics at La Reunion hot spot. Three depth-dependent magmatic differentiation stages of a single transitional parental magma (9–11 wt% MgO and 0.5–0.8 wt% K₂O) may account for the entire range of major element compositions in products from the Piton de la Fournaise volcano. The deepest differentiation (>7.5 km) consists in the fractional crystallization of clinopyroxene + plagioclase, explaining occurrences of “abnormal eruptions” and gabbros throughout the island. The most abundant volcanic products are formed at shallower depth (<2.5 km), by olivine-controlled differentiation of the transitional parental magma. Olivine fractional crystallization yields a vertical chemical stratification of the magma storage zone, with differentiated basalts at the top and picrites at the base of the reservoir. Differentiated basalts may themselves evolve beneath the surface (<0.6 km) into more differentiated melts by clinopyroxene + plagioclase fractionation. This superposition of three differentiation processes is consistent with the existence of three magmatic systems interpreted from geophysical studies. Unlike previous studies, we suggest that magma mixing or incorporation of dunite xenoliths are not necessary to explain the major element chemical diversity of Piton de la Fournaise rocks. Because the major element composition of Piton de la Fournaise products is representative of other OIBs in the Indian Ocean, successive differentiation stages of a single homogeneous magma at >7.5 km, <2.5 km, and underneath the surface might be the rule rather than the

exception. Our study shows that combining whole rock, melt inclusion, gas inclusion and matrix glass data is critical to constrain the full range of magma differentiation processes. Taken separately, each data set only yields an incomplete history, whereas taken together, they provide a more robust framework for interpreting the complete evolution of a volcanic edifice.

Acknowledgments

[38] We thank Glenn Gaetani, Stephanie Ingle, and an anonymous reviewer for greatly improving the quality of the manuscript. This work was supported by grants from the Conseil Régional de la Réunion. This is IGP contribution 2423.

References

- Albarède, F., and V. Tamagnan (1988), Modelling the recent geochemical evolution of the Piton de la Fournaise volcano, Réunion Island, *J. Petrol.*, **29**, 997–1030.
- Albarède, F., B. Luais, G. Fitton, M. P. Semet, E. Kaminski, B. G. J. Upton, P. Bachèlery, and J. L. Cheminée (1997), The geochemical regimes of Piton de la Fournaise Volcano (Réunion) during the last 530,000 years, *J. Petrol.*, **38**, 171–201, doi:10.1093/petrology/38.2.171.
- Asimow, P. D., and M. S. Ghiorso (1998), Algorithmic modifications extending MELTS to calculate subsolidus phase relations, *Am. Mineral.*, **83**, 1127–1131.
- Barnes, S. J., and P. L. Roeder (2001), The range of spinel compositions in terrestrial mafic and ultramafic rocks, *J. Petrol.*, **42**, 2279–2302, doi:10.1093/petrology/42.12.2279.
- Battaglia, J., K. Aki, and V. Ferrazzini (2005a), Location of tremor source and estimation of lava output using tremor source amplitude on the Piton de La Fournaise volcano: 1. Location of tremor sources, *J. Volcanol. Geotherm. Res.*, **147**(3–4), 268–290, doi:10.1016/j.jvolgeores.2005.04.005.
- Battaglia, J., V. Ferrazzini, T. H. Staudacher, K. Aki, and J. L. Cheminée (2005b), Pre-eruptive migration of earthquakes at the Piton de la Fournaise volcano (Réunion Island), *Geophys. J. Int.*, **161**, 549–558, doi:10.1111/j.1365-246X.2005.02606.x.
- Bence, A. E., and A. L. Albee (1968), Empirical correction factors for the electron microanalysis of silicates and oxides, *J. Geol.*, **76**, 382–403.
- Bosch, D., J. Blichert-Toft, F. Moynier, B. K. Nelson, P. Telouk, P.-Y. Gillot, and F. Albarède (2008), Pb, Hf and Nd isotope compositions of the two Réunion volcanoes (Indian Ocean): A tale of two small-scale mantle “blobs”?, *Earth Planet. Sci. Lett.*, **265**(3–4), 748–768, doi:10.1016/j.epsl.2007.11.018.
- Bureau, H., N. Métrich, F. Pineau, and M. P. Semet (1998a), Magma-conduit interaction at Piton de la Fournaise volcano (Réunion Island): A melt and fluid inclusion study, *J. Volcanol. Geotherm. Res.*, **84**, 39–60, doi:10.1016/S0377-0273(98)00029-8.
- Bureau, H., F. Pineau, N. Métrich, M. P. Semet, and M. Javoy (1998b), A melt and fluid inclusion study of the gas phase at Piton de la Fournaise volcano (Réunion Island), *Chem. Geol.*, **147**(1–2), 115–130, doi:10.1016/S0009-2541(97)00176-9.
- Bureau, H., N. Métrich, M. P. Semet, and T. Staudacher (1999), Fluid-magma decoupling in a hot-spot volcano, *Geophys. Res. Lett.*, **26**(23), 3501–3504, doi:10.1029/1999GL005422.
- Chen, C.-Y., and F. A. Frey (1983), Origin of Hawaiian tholeiite and alkalic basalt, *Nature*, **302**, 785–789, doi:10.1038/302785a0.
- Chevallier, L., and N. Vatin-Perignon (1982), Volcano-structural evolution of Piton des Neiges, Reunion Island, Indian Ocean, *Bull. Volcanol.*, **45**(4), 285–298, doi:10.1007/BF02597253.
- Clocchiatti, R., A. Havette, and P. Nativel (1979), Relations pétrogénétiques entre les basaltes transitionnels et les océanites du Piton de la Fournaise (île de la Réunion, Océan Indien) à partir de la composition chimique des inclusions vitreuses des olivines et des spinelles, *Bull. Mineral.*, **102**, 511–525.
- Danyushevsky, L. V., F. N. Della-Pasqua, and S. Sokolov (2000), Re-equilibration of melt inclusions trapped by magmatic olivine phenocrysts from subduction-related magmas: Petrological implications, *Contrib. Mineral. Petrol.*, **138**, 68–83, doi:10.1007/PL00007664.
- Danyushevsky, L. V., R. A. J. Leslie, A. J. Crawford, and P. Durand (2004), Melt inclusions in primitive olivine phenocrysts: The role of localized reaction processes in the origin of anomalous compositions, *J. Petrol.*, **45**, 2531–2553, doi:10.1093/petrology/egh080.
- Debajyoti, P., V. S. Kamenetsky, A. W. Hofmann, and A. Stracke (2007), Compositional diversity among primitive lavas of Mauritius, Indian Ocean: Implications for mantle sources, *J. Volcanol. Geotherm. Res.*, **164**, 76–94, doi:10.1016/j.jvolgeores.2007.04.004.
- Faure, F., and P. Schiano (2005), Experimental investigation of equilibration conditions during forsterite growth and melt inclusion formation, *Earth Planet. Sci. Lett.*, **236**(3–4), 882–898, doi:10.1016/j.epsl.2005.04.050.
- Fisk, M. R., B. G. J. Upton, C. E. Ford, and W. M. White (1988), Geochemical and experimental study of the genesis of magmas of Réunion Island, Indian Ocean, *J. Geophys. Res.*, **93**(B5), 4933–4950, doi:10.1029/JB093iB05p04933.
- Gaetani, G. A., and E. B. Watson (2000), Open system behavior of olivine-hosted melt inclusions, *Earth Planet. Sci. Lett.*, **183**(1–2), 27–41, doi:10.1016/S0012-821X(00)00260-0.
- Gaetani, G. A., and E. B. Watson (2002), Modeling the major-element evolution of olivine-hosted melt inclusions, *Chem. Geol.*, **183**, 25–41, doi:10.1016/S0009-2541(01)00370-9.
- Ghiorso, M. S., and R. O. Sack (1995), Chemical mass transfer in magmatic processes. IV. A revised and internally consistent thermodynamic model for the interpolation and extrapolation of liquid-solid equilibria in magmatic systems at elevated temperatures and pressures, *Contrib. Mineral. Petrol.*, **119**, 197–212, doi:10.1007/BF00307281.
- Green, D. H., and A. E. Ringwood (1967), The genesis of basaltic magmas, *Contrib. Mineral. Petrol.*, **15**, 103–190, doi:10.1007/BF00372052.
- Hansteen, T. H., A. Klügel, and H.-U. Schmincke (1998), Multi-stage magma ascent beneath the Canary Islands: Evidence from fluid inclusions, *Contrib. Mineral. Petrol.*, **132**(1), 48–64, doi:10.1007/s004100050404.
- Hauri, E. H. (1992), Major-element variability in the Hawaiian mantle plume, *Nature*, **382**, 415–419, doi:10.1038/382415a0.
- Helz, R. T., and C. R. Thornber (1987), Geothermometry of Kilauea Iki lava lake Hawaii, *Bull. Volcanol.*, **49**, 651–668, doi:10.1007/BF01080357.
- Thinger, P. D., R. L. Hervig, and P. F. McMillan (1994), Analytical methods for volatiles in glasses, *Rev. Mineral. Geochem.*, **30**(1), 67–121.

- Kawakami, Y., J. Yamamoto, and K. Hiroyuki (2003), Micro-Raman densimeter for CO₂ inclusions in mantle-derived minerals, *Appl. Spectrosc.*, **57**(11), 1333–1339, doi:10.1366/00037020322554473.
- Kornprobst, J., P. Boivin, and P. Bachèlery (1979), L'alimentation des éruptions récentes du Piton de la Fournaise (Ile de la Réunion, Océan Indien): Degré d'évolution et niveau de ségrégation des laves émises, *C. R. Acad. Sci.*, **288D**(29), 1691–1694.
- Lacroix, A. (1936), *Le Volcan Actif de l'île de la Réunion et ses Produits*, Gauthier-Villard, Paris.
- Lénat, J. F., and P. Bachèlery (1990), Structure et fonctionnement de la zone centrale du Piton de La Fournaise, in *Le Volcanisme de La Réunion*, edited by J. F. Lénat, pp. 257–296, Cent. de Rech. Volcanol., Clermont-Ferrand, France.
- Lister, J. R., and R. C. Kerr (1991), Fluid-mechanical models of crack propagation and their application to magma transport in dykes, *J. Geophys. Res.*, **96**(B6), 10,049–10,077, doi:10.1029/91JB00600.
- Longpré, M.-A., T. Staudacher, and J. Stix (2007), The November 2002 eruption at Piton de la Fournaise volcano, La Réunion Island: Ground deformation, seismicity, and pit crater collapse, *Bull. Volcanol.*, **69**, 511–525, doi:10.1007/s00445-006-0087-0.
- Luais, B. (2004), Temporal changes in Nd isotopic composition of Piton de la Fournaise magmatism (Réunion Island, Indian Ocean), *Geochem. Geophys. Geosyst.*, **5**, Q01008, doi:10.1029/2002GC000502.
- Ludden, J. N. (1978), Magmatic evolution of the basaltic shield volcanoes of Réunion Island, *J. Volcanol. Geotherm. Res.*, **4**, 171–198, doi:10.1016/0377-0273(78)90035-5.
- Macdonald, G. A., and T. Katsura (1964), Chemical composition of Hawaiian lavas, *J. Petrol.*, **5**, 82–133.
- Maurel, C., and P. Maurel (1982), Etude expérimentale de l'équilibre Fe²⁺-Fe³⁺ dans les spinelles chromifères et les liquides silicatés basiques coexistants à 1 atm., *C. R. Acad. Sci.*, **295**(II), 209–212.
- Mohamed-Abchir, A., M. P. Semet, G. Boudon, P. Ildefonse, P. Bachèlery, and R. Clocchiatti (1998), Huge hydrothermal explosive activity on Piton de la Fournaise, Réunion Island: The Bellecombe Ash Member, 2700 BC, in *The European Laboratory Volcanoes, Proceedings of the Second Workshop, 2 to 4 May 1996*, pp. 447–455, Luxembourg Off. for Off. Publ. of the Eur. Communities, Santorini, Greece.
- Morgan, G. B. VI, and D. London (1996), Optimizing the electron microprobe analysis of hydrous alkali aluminosilicate glasses, *Am. Mineral.*, **81**, 1176–1185.
- Newman, S., and J. B. Lowenstern (2002), VOLATILECALC: A silicate melt-H₂O-CO₂ solution model written in Visual Basic for Excel, *Comput. Geosci.*, **28**, 597–604, doi:10.1016/S0098-3004(01)00081-4.
- Oversby, V. M. (1972), Genetic relations among the volcanic rocks of Réunion: Chemical and lead isotopic evidence, *Geochim. Cosmochim. Acta*, **36**, 1167–1179, doi:10.1016/0016-7037(72)90097-X.
- Peltier, A., V. Famin, P. Bachèlery, V. Cayol, Y. Fukushima, and T. H. Staudacher (2008), Cyclic magma transports at Piton de La Fournaise volcano (La Réunion hotspot) inferred from deformation and geochemical data, *Earth Planet. Sci. Lett.*, **270**(3–4), 180–188.
- Peterson, D. W., and R. B. Moore (1987), Geologic history and evolution of geologic concepts, island of Hawaii, *U. S. Geol. Surv. Prof. Pap.*, **1350**, 149–189.
- Rançon, J. P., P. Rocher, T. Auge, and P. Nativel (1988), Pétrologie de deux complexes intrusifs lités de l'île de la Réunion, Implications volcano-structurales, *Geol. Fr.*, **2–3**, 135–156.
- Ren, Z.-Y., S. Ingle, E. Takahashi, N. Hirano, and T. Hirata (2005), The chemical structure of the Hawaiian mantle plume, *Nature*, **436**, 837–840, doi:10.1038/nature03907.
- Rhodes, J. M. (1988), Geochemistry of the 1984 Mona Loa eruption: Implication for magma storage and supply, *J. Geophys. Res.*, **93**, 4453–4466, doi:10.1029/JB093iB05p04453.
- Roedder, E. (1979), Origin and significance of magmatic inclusions, *Bull. Mineral.*, **102**, 457–510.
- Roedder, E. (1984), *Fluid Inclusions*, *Rev. in Mineral.*, vol. 12, 644 pp., Mineral. Soc. of Am., Chantilly, Va.
- Ryan, M. P. (1988), The mechanics and three-dimensional internal structure of active magmatic systems: Kilauea Volcano, Hawaii, *J. Geophys. Res.*, **93**(B5), 4213–4248, doi:10.1029/JB093iB05p04213.
- Schiano, P., A. Provost, R. Clocchiatti, and F. Faure (2006), Transcrystalline melt migration and Earth's mantle, *Science*, **314**, 970–974, doi:10.1126/science.1132485.
- Sobolev, A., A. W. Hofmann, S. V. Sobolev, and I. K. Nikogosian (2005), An olivine-free mantle source of Hawaiian shield basalts, *Nature*, **434**, 590–597, doi:10.1038/nature03411.
- Sours-Page, R., R. L. Nielsen, and R. Batiza (2002), Melt inclusions as indicators of parental magma diversity on the northern East Pacific Rise, *Chem. Geol.*, **183**, 237–261, doi:10.1016/S0009-2541(01)00384-9.
- Tilley, C. E., R. N. Thompson, W. J. Wadsworth, and B. G. J. Upton (1971), Melting relations of some lavas of Réunion Island, Indian Ocean, *Mineral. Mag.*, **38**, 344–352, doi:10.1180/minmag.1971.038.295.09.
- Upton, B. G. J., and W. J. Wadsworth (1965), Geology of Réunion Island, Indian Ocean, *Nature*, **207**, 151–154, doi:10.1038/207151a0.
- Upton, B. G. J., and W. J. Wadsworth (1972a), Aspects of magmatic evolution on Réunion Island, *Philos. Trans. R. Soc. London, Ser. A*, **271**, 105–130.
- Upton, B. G. J., and W. J. Wadsworth (1972b), Peridotitic and gabbroic rocks associated with the Shield-Forming lavas of Réunion, *Contrib. Mineral. Petrol.*, **35**, 139–158, doi:10.1007/BF00370925.
- Upton, B. G. J., M. P. Semet, and J.-L. Joron (2000), Cumulate clasts in the Bellecombe Ash Member, Piton de la Fournaise, Réunion Island, and their bearing on cumulative processes in the petrogenesis of the Réunion lavas, *J. Volcanol. Geotherm. Res.*, **104**(1–4), 297–318, doi:10.1016/S0377-0273(00)00212-2.
- Villeneuve, N. (2000), Apports multi-sources à une meilleure compréhension de la mise en place des coulées de lave et des risques associés au Piton de la Fournaise, Ph.D. thesis, Univ. Pierre et Marie Curie, Paris.
- Vlastélic, I., T. Staudacher, and M. Semet (2005), Rapid change of lava composition from 1998 to 2002 at Piton de La Fournaise (Réunion) inferred from Pb isotopes and trace elements: Evidence for variable crustal contamination, *J. Petrol.*, **46**, 79–107, doi:10.1093/petrology/egh062.
- Vlastélic, I., A. Peltier, and T. Staudacher (2007), Short-term (1998–2006) fluctuations of Pb isotopes at Piton de la Fournaise volcano (Réunion Island): Origins and constraints on the size and shape of the magma reservoir, *Chem. Geol.*, **244**, 202–220, doi:10.1016/j.chemgeo.2007.06.015.
- Zielinski, R. A. (1975), Trace element evaluation of a suite of rocks from Réunion island, Indian Ocean, *Geochim. Cosmochim. Acta*, **39**, 713–734, doi:10.1016/0016-7037(75)90012-5.